hydrology

MDPI

Article

Hydrological and Hydrodynamic Responses to High-Resolution Diffusion-Enhanced Radar Rainfall Forcing in a Floodplain Reach of the Middle Yangtze River

Dian Feng [1,2,*], Shaoni Huang [2], Yibo Du [2], Lihao Zhou [3] and Jun Zhang [4,5,*]

1 Heavy Rainfall Research Center of China, Wuhan Institute of Heavy Rain, China Meteorological Administration, Wuhan 430205, China
2 Shaanxi Meteorological Bureau, Xi'an 710014, China; hsn_met@163.com (S.H.); duyb521@163.com (Y.D.)
3 School of Water Resources and Hydropower Engineering, Wuhan University, Wuhan 430072, China; leozhou@whu.edu.cn
4 Hubei Key Laboratory of Intelligent Yangtze and Hydroelectric Science, China Yangtze Power Co., Ltd., Yichang 443000, China
5 Yangtze Ecology and Environment Co., Ltd., Wuhan 430062, China
* Correspondence: fengdian94@163.com (D.F.); zhang_jun20@ctg.com.cn (J.Z.)

Abstract

Flash-flood and floodplain inundation simulations are highly sensitive to the spatiotemporal variability of convective rainfall, particularly during the initial runoff generation stage. However, coarse-resolution numerical weather prediction (NWP) forcing tends to smooth localized rainfall extremes, limiting its ability to accurately represent hydrological responses in low-relief floodplains. In this study, we couple a diffusion-enhanced radar nowcasting model, Diff_ConvLSTM, with a spatial resolution of 1 km and a temporal resolution of 6 min, to assess the hydrological value of high-resolution rainfall forcing over the middle Yangtze River floodplain. We introduce a monotone piecewise cubic Hermite interpolation scheme to ensure a stable transition from discrete high-frequency rainfall inputs to continuous hydrodynamic integration. Evaluation using a radar dataset from 2023 to 2024 shows that Diff_ConvLSTM better preserves intense convective echoes and rainband structures compared to the baseline ConvLSTM, increasing the Probability of Detection at the 40 dBZ threshold by 65.8%. A forcing-replacement experiment for the flood event on 30 June 2023 demonstrates that AI-based nowcasting rainfall forcing reduces peak-discharge underestimation, improves volumetric consistency, and produces inundation patterns that are closer to the observation-driven reference than those generated by low-resolution forecast forcing, although positive biases in inundation area and water depth persist. An additional event in 2024 confirms that the improvements are primarily reflected in discharge magnitude and flood volume representation, while enhancements in peak timing remain limited. Overall, the results illustrate both the added value and the remaining limitations of AI-enhanced nowcasting for hydrologically informed flood forecasting.

Keywords: radar nowcasting; hydrological response; floodplain inundation; rainfall forcing; TELEMAC-2D

Check for updates

Academic Editors: Hao Han and Aristoteles Tegos

Received: 17 April 2026
Revised: 28 May 2026
Accepted: 29 May 2026
Published: 30 May 2026

Copyright: © 2026 by the authors. Licensee MDPI, Basel, Switzerland. This article is an open access article distributed under the terms and conditions of the Creative Commons Attribution (CC BY) license.

1. Introduction

Short-duration convective precipitation is increasingly recognized as a major trigger of rapidly evolving flood hazards in low-lying floodplains and small-to-medium catchments [1,2]. Owing to its strong spatial heterogeneity and rapid temporal variability, flood

responses are often highly sensitive to rainfall structures at kilometer and minute scales. In particular, the timing and magnitude of peak discharge, as well as the spatial distribution of inundation depth, can be strongly affected by localized rainfall variability.

Operational flood forecasting systems commonly rely on precipitation products from numerical weather prediction (NWP) models to drive hydrological or hydrodynamic simulations [3–5]. However, at convective scales, coarse temporal resolution and spatial smoothing may weaken local extremes and distort rainband structure. When such rainfall fields are used as external forcing, the resulting errors can be further amplified through runoff generation, flow routing, and ultimately degrading the simulation of peak discharge, hydrograph shape, and floodplain inundation.

Precipitation nowcasting is generally applicable to 0–3 h lead times and gives short-lead rainfall information which is hard to obtain from standard NWP products [6–8]. The ability to replicate the rapid development of convective systems is a key strength of the model [9,10]. End-to-end spatiotemporal modeling studies, particularly those based on ConvLSTM architectures, have become increasingly important in radar-based nowcasting [11–13]. The primary rainband advection is generally well reproduced by these models [14,15]. Notwithstanding, their deterministic formulation continues to be a drawback in strong convective situations. Forecasts usually exhibit too much smoothing that quickly weakens high-reflectivity cores and removes fine-scale precipitation features [16,17]. When it comes to capturing the localized extremes of rainfall accurately, these limitations become important rather than just the large-scale relocation of system precipitation.

Previous studies have demonstrated that the spatiotemporal organization of rainfall plays a critical role in controlling hydrological responses. Paschalis et al. [18] illustrated that small-scale rainfall variability can significantly influence basin flood responses, particularly in terms of flood-peak magnitude and timing. Furthermore, Saharia et al. [19] revealed that the spatial organization of rainfall affects flash-flood severity to a degree comparable to geomorphology and climatology. These findings suggest that the hydrological impact of rainfall forcing depends not only on the total amount of rainfall but also on the spatial concentration, temporal continuity, and movement of intense rainfall structures.

In terms of hydrodynamics, high-resolution two-dimensional (2D) shallow-water solvers such as TELEMAC-2D are capable of a physical description of floodplain flow and inundation under complex topography and boundary conditions [20–22]. Due to its rain-on-grid capability, inherently distributed rainfall forcing can be directly applied to the computational mesh, thus providing a practical interface for meteorology–hydrodynamics coupling [23–26]. Nevertheless, a major issue is reconciling the continuous time integration of hydrodynamic solvers with their discrete high-frequency rainfall inputs. If the forcing interval is much larger than the solver time step, the solution may introduce non-physical oscillations or become unstable [27–29].

Simultaneously, diffusion-based generative modeling has recently emerged as a new approach for improving the structural realism of short-term precipitation forecasts. Diffusion-enhanced approaches explicitly model uncertainties in residuals conditioned on a deterministic trend, reducing over-smoothing of convective cores and better preserving multi-scale rainband structures. This feature is especially useful in flood forecasting applications where simulations need to be purely reliant on predictive rainfall forcing, in the absence of any observations.

In response to this gap, we propose an integrated flood forecasting framework that links diffusion-enhanced precipitation nowcasting with TELEMAC-2D. Rather than relying on stepwise forcing, the framework employs a shape-preserving interpolation scheme to ensure a smooth transition from discrete rainfall inputs to continuous hydrodynamic routing. In addition, a forcing-replacement experiment aims to isolate the end-to-end

hydrodynamic effect of early rainfall forecast errors. We demonstrate that the introduction of AI nowcasting based on diffusion models reduces the underestimation of convective extremes, resulting in more realistic forecasts of flood peaks and inundation processes in operational settings.

The remainder of this paper is organized as follows: Section 2 outlines the materials and methods, including a description of the study area, data sources, the diffusion-enhanced nowcasting model, the TELEMAC-2D hydrodynamic model, and the experimental design for forcing replacement. Section 3 presents the empirical results for both precipitation nowcasting and hydrodynamic simulations. Section 4 discusses the main findings, methodological innovations, and limitations of the study, while Section 5 summarizes the conclusions drawn from this research.

2. Materials and Methods

2.1. Study Area

The study area covers the middle Yangtze River reach between Shishou and Jianli and its adjacent contributing region (Figure 1). It is located within the Jianghan Plain, characterized by low relief, subtle topographic gradients, and a dense network of rivers and lakes. During the main flood season (April–October), precipitation is influenced by both the Meiyu frontal system and mesoscale convective activity [30,31], leading to rainfall with high intensity, rapid temporal variability, and pronounced spatial heterogeneity. In this low-lying floodplain setting, the interaction between localized convective extremes and complex surface conditions plays a key role in controlling runoff generation and subsequent flood evolution. These characteristics make the region well suited for evaluating the coupling of high-resolution precipitation nowcasting and hydrodynamic modeling.

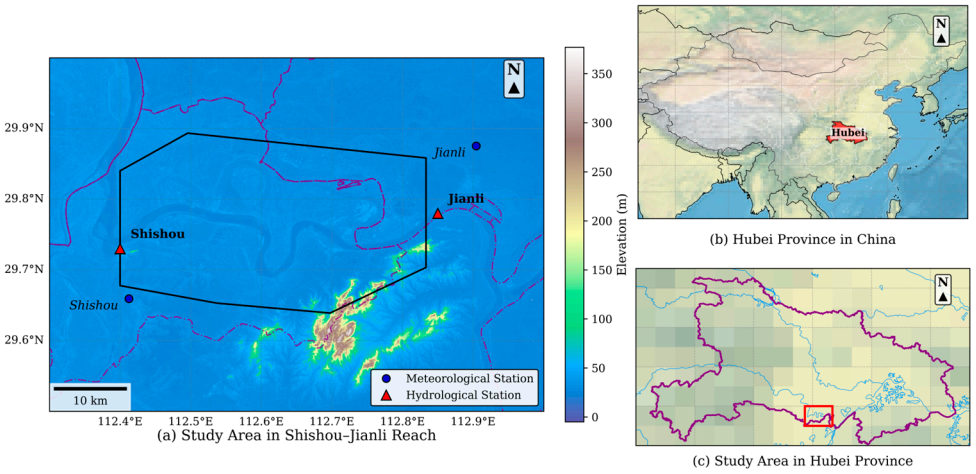


Figure 1. Spatial distribution of meteorological and hydrological stations in the Jingjiang reach of the Yangtze River Basin (the background shows DEM elevation; blue dots indicate meteorological stations; red triangles indicate hydrological stations; the black solid line denotes the hydrodynamic modeling boundary).

The hydrodynamic computational domain established for the Shishou–Jianli reach encompasses a total area of approximately 993.13 km^2. This domain comprehensively includes the main river channel, adjacent low-lying floodplains, local drainage networks, and areas prone to chronic inundation, which are characteristic of the middle Yangtze River Basin.

Utilizing the ALOS World 3D–30 m (AW3D30) digital elevation dataset, the surface topography across the domain reveals an absolute elevation range from 6 to 335 m, with a mean elevation of 35.41 m. The macro-topography is predominantly flat and gentle,

exhibiting a mean land surface slope of 5.44%. The 25th, 50th, and 75th percentiles of the slope distribution are 1.85%, 3.71%, and 6.74%, respectively. These statistics quantitatively confirm that the study area is structurally dominated by the low-relief floodplain morphology of the Jianghan Plain, while local topographic gradients are primarily influenced by artificial river embankments, minor hydraulic structures, and adjacent highlands.

2.2. Data Sources

To construct the TELEMAC-2D computational domain, we used the ALOS World 3D–30 m (AW3D30) dataset as the base terrain data (https://www.eorc.jaxa.jp/ALOS/en/dataset/aw3d30/aw3d30_e.htm, accessed on 15 April 2026) [32], and the annual 30 m China land-cover dataset (https://zenodo.org/records/15853565, accessed on 15 April 2026) [33,34]. Following the reference roughness table in the *Hydraulic Calculation Manual* (2nd edition) [35], an initial Manning's n was assigned to each land-cover type, and spatially distributed roughness and infiltration parameters were then specified across the computational mesh, as detailed in the model parameterization section (Section 2.6). Boundary conditions, as well as calibration and validation data, are mainly derived from continuous water-level and discharge observations at the Shishou and Jianli hydrological stations during 2023–2024 (these data were provided by Yangtze Ecology and Environment Co., Ltd.). These multi-source datasets jointly supported terrain construction, parameterization, model calibration, validation, and performance evaluation.

The training of the nowcasting model and the preparation of hydrodynamic forcing rely on accurate and spatiotemporally continuous precipitation inputs. Therefore, two sets of data were selected as precipitation forcing in this study: (1) surface station observations and (2) high-quality radar reflectivity composites. The surface station data are derived from the National Basic Meteorological Element Dataset Product V3.0 (http://www.nmic.cn/, accessed on 15 April 2026). The latter, the radar composite, offers the critical advantage of capturing the fine-scale spatial heterogeneity and rapid dynamics of convective storms, which are often missed by sparse gauge networks. The radar composite has a spatial resolution of 1 km and a temporal resolution of 6 min, covering the domain of 111–115° E and 29–32° N (the national radar mosaic dataset was archived and provided by the China Meteorological Administration). Before analysis, the product undergoes an automatic quality-control procedure that removes clutter, corrects for blockage and attenuation, filters out weak-echo noise, and reprojects the data onto a common Cartesian grid.

2.3. Diffusion-Enhanced Precipitation Nowcasting Model

The strong nonlinearity of convective evolution makes radar echo extrapolation and precipitation nowcasting challenging for spatio-temporal forecasting problems [11,12,16,17]. At longer lead times, traditional methods predominantly recreate straightforward rainband translation with limited capabilities in accurately depicting convective cell development, merging, and dissipation [12,17]. As such, regions of high reflectivity weaken too rapidly, and small-scale features are too blurred [16]. To counteract the over-smoothing effect in deterministic predictions, we use a dual-branch framework based on DiffCast [36], which employs a deterministic trend and a stochastic diffusion residual. In this way, we alleviate the over-smoothing caused by only using a deterministic prediction. In particular, the technique of conditional diffusion residual modeling is incorporated into a deterministic baseline framework powered by ConvLSTM, leading to the formation of schema Diff_ConvLSTM. Figure 2 depicts a diagrammatic representation of the training modeling constructed.

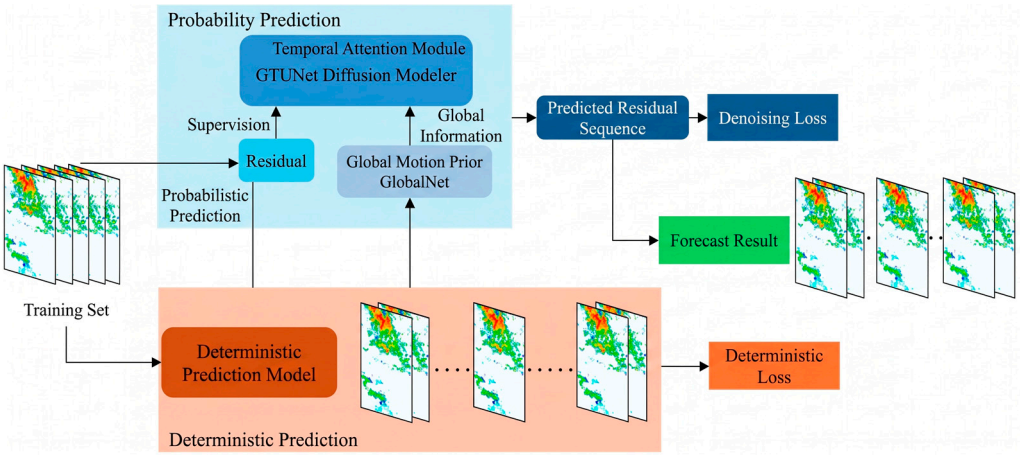


Figure 2. The overview of Diff_ConvLSTM framework for precipitation nowcasting (Blue blocks: probability prediction; Orange blocks: deterministic prediction; Green block: forecast result).

2.3.1. ConvLSTM

The ConvLSTM (Convolutional Long Short-Term Memory) network is utilized to integrate the spatial feature extraction capabilities of convolutional neural networks with the temporal retention mechanisms of LSTMs [11,12]. For precipitation nowcasting, ConvLSTM applies spatial convolutions across continuous radar image sequences and recursively updates its hidden states, thereby accurately characterizing the spatiotemporal dynamics and advection processes of convective rainfall.

$$i_t = \sigma(W_{xi} * X_t + W_{hi} * H_{t-1} + b_i), \tag{1}$$

$$f_t = \sigma\left(W_{xf} * X_t + W_{hf} * H_{t-1} + b_f\right), \tag{2}$$

$$o_t = \sigma(W_{xo} * X_t + W_{ho} * H_{t-1} + b_o), \tag{3}$$

$$\widetilde{C}_t = tanh(W_{xc} * X_t + W_{hc} * H_{t-1} + b_c) \tag{4}$$

$$C_t = f_t \odot C_{t-1} + i_t \odot \widetilde{C}_t, \tag{5}$$

$$H_t = o_t \odot tanh(C_t). \tag{6}$$

where X_t is the input radar echo at time t, H_{t-1} is the hidden state at the previous time step, and C_t is the cell state. i_t, f_t, and o_t denote the input, forget, and output gates, respectively; $\widetilde{C}_t$ is the candidate cell state; $*$ denotes the convolution operation; $\odot$ denotes the Hadamard product; and $\sigma(\cdot)$ is the sigmoid activation function.

During training, the model parameters are optimized using a pixel-wise mean squared error (MSE) loss between the prediction and observation radar echo sequences [12,13]. Although ConvLSTM reproduces the overall motion of precipitation systems, it often offers overly smooth results and weakened high-reflectivity centers under severe convective conditions. Therefore, in this study, ConvLSTM is regarded as the deterministic baseline, and its limitations are further compensated by the subsequent diffusion-based residual module.

2.3.2. Diff_ConvLSTM Training Framework

The Diff_ConvLSTM framework is formulated as a two-stage generative paradigm that integrates a deterministic prediction of large-scale advection with a stochastic diffusion process for fine-scale texture recovery, thus facilitating the mitigation of over-smoothing issues inherent in purely deterministic models by capturing both the macro-scale evolution and the micro-scale stochasticity of precipitation [13,16,17,37].

In the first stage, the deterministic branch utilizes a ConvLSTM to generate a prior prediction μ_t for time t, focusing on capturing the spatiotemporal movement and morphological characteristics of the rainband. Subsequently, the residual extraction phase identifies the discrepancy between the ground truth X_t and this prior prediction, defining the residual as $r_t = X_t - \mu_t$.

The second stage involves the stochastic diffusion branch, where a Global Temporal U-Net (GTUNet) is employed for conditional diffusion modeling of the residual sequence [37]. During the forward diffusion process, Gaussian noise is incrementally added to the residual r_t over t steps, and the distribution of the noisy residual at step k is given by

$$q\left(r_t^{(k)} \middle| r_t\right) = \mathcal{N}\left(\sqrt{\bar{\alpha}_k} r_t, (1 - \bar{\alpha}_k) I\right) \tag{7}$$

In the reverse denoising process, the network ϵ_θ is trained to recover the residual from the noise, guided by the global prior condition $\mu_{1:T}$. The reverse transition probability is defined as

$$p_\theta\left(r_t^{(k-1)} \middle| r_t^{(k)}, \mu_{1:T}\right) = \mathcal{N}\left(\mu_\theta, \sigma_k^2 I\right) \tag{8}$$

Finally, through the fused output module, the refined residual r_t generated via the reverse diffusion process is added back to the deterministic prior μ_t to produce the final precipitation field $X_t = \mu_t + r_t$. To jointly optimize both branches, the overall loss function is defined as a weighted sum of a deterministic MSE term and a diffusion term:

$$\mathcal{L} = \underbrace{\mathrm{MSE}(\mu_t, X_t)}_{\text{certainty}} + \underbrace{\alpha \mathbb{E}_k \|\varepsilon_\theta\left(r_t^{(k)}, k, \mu_{1:T}\right) - \varepsilon\|_2^2}_{\text{Diffsuion}} \tag{9}$$

where α controls the trade-off between deterministic trajectory accuracy and the reconstruction of fine-scale stochastic details. Within this framework, the deterministic prediction serves as a reliable motion prior, while the diffusion branch models the intrinsic uncertainty and texture variability of convective systems. The implementation settings follow the original DiffCast architecture.

2.4. TELEMAC-2D Hydrodynamic Model

In this study, the two-dimensional hydrodynamic model TELEMAC-2D (version 9.0) [20] is used to simulate the rainfall–runoff generation, overland flow, and flood routing in the channel. The model solves the two-dimensional shallow-water equations (SWEs) on unstructured triangular meshes, and it supports both the finite element and finite volume formulations [21,23,38,39]. Compared to one-dimensional routing models or simplified kinematic-wave schemes, the new 2D shallow-water framework for floodplain hydraulics offers a more physically complete description, especially where backwater interactions and flow-regime transitions are important.

The governing equations, consisting of the continuity and momentum equations, are expressed as follows:

$$\frac{\partial h}{\partial t} + u\frac{\partial h}{\partial x} + v\frac{\partial h}{\partial y} + h\left(\frac{\partial u}{\partial x} + \frac{\partial v}{\partial y}\right) = S_h \tag{10}$$

$$\frac{\partial u}{\partial t} + u\frac{\partial u}{\partial x} + v\frac{\partial u}{\partial y} = -g\frac{\partial Z}{\partial x} + S_x + \frac{1}{h}\nabla \cdot (h\nu_t \nabla u) \tag{11}$$

$$\frac{\partial v}{\partial t} + u\frac{\partial v}{\partial x} + v\frac{\partial v}{\partial y} = -g\frac{\partial Z}{\partial y} + S_y + \frac{1}{h}\nabla \cdot (h\nu_t \nabla v) \tag{12}$$

where h denotes the water depth; u and v are the depth-averaged horizontal velocity components; Z represents the absolute free surface elevation, defined as the sum of the bed elevation and water depth ($Z = Z_f + h$); g is the gravitational acceleration; and ν_t signifies the turbulent viscosity coefficient responsible for momentum mixing.

In the "rain-on-grid" configuration, the continuity source term signifies the net rainfall forcing applied to each computational cell. This study employs the SCS-CN runoff module integrated within TELEMAC-2D to represent infiltration and runoff generation. The spatially distributed curve number field is derived from land cover and soil type information, which is then mapped onto the unstructured computational mesh. Additionally, the momentum source terms incorporate bed friction, wind shear stress, and Coriolis forcing.

2.5. Monotone Temporal Interpolation for Rainfall–Hydrodynamic Coupling

The high-resolution AI rainfall forecast is temporally coupled into the TELEMAC-2D hydrodynamic model. Rainfall inputs are provided at 6 min intervals, while the hydrodynamic solver is typically run at second or sub-second time steps to satisfy the Courant–Friedrichs–Lewy (CFL) stability condition. When the rainfall series is applied directly in a stepwise manner, sharp temporal discontinuities are introduced in the shallow-water equations. This unexpected forcing may produce non-physical "numerical shocks" and affect solver stability, especially near wet–dry interfaces and during flux computation using Riemann solvers [27]. Despite the fact that classical cubic spline interpolation is capable of smoothing the discrete rainfall sequence, the classical cubic spline interpolation has the potential to generate the Runge effect. This means that the interpolation will overshoot from below to above the actual values, generating artificial oscillations between two successive temporal nodes [40]. In conditions where convective activity is strong, the rainfall intensity may fluctuate sharply. The use of high-degree polynomials in such conditions can lead to undesired effects like "overshoot" and spurious oscillations. This can lead to a physical manifestation of erroneous negative precipitation and mass-conservation violations [40]. The use of spatially distributed rainfall forcing aligns with contemporary studies in rain-on-grid hydrodynamic modeling. Costabile et al. [41] proposed a stochastic rain-on-grid framework that connects spatiotemporal uncertainties in rainfall with the two-dimensional hydrodynamic impacts for flood nowcasting. In contrast to stochastic rainfall generation, this study emphasizes the application of AI-based high-resolution rainfall nowcasting as the dynamic forcing source. Nonetheless, both methodologies underscore the importance of maintaining the structure of rainfall for effective impact-oriented flood simulations.

To ensure a seamless and physically consistent transition from meteorological forcing to the hydrodynamic environment, this study implements the Fritsch–Carlson monotonic shape-preserving piecewise cubic Hermite interpolation algorithm [40,42,43]. By imposing strict nonlinear constraints on the tangent slope m_k of the precipitation sequence (t_k, P_k) at each temporal node, the algorithm ensures that the resulting interpolation function $P_{smooth}(t)$ strictly preserves the monotonicity of the original data. The governing interpolation equation for a given interval $[t_k, t_{k+1}]$ is defined as follows:

$$P_{smooth}(t) = \left(2s^3 - 3s^2 + 1\right)P_k + h_k\left(s^3 - 2s^2 + s\right)m_k + \left(-2s^3 + 3s^2\right)P_{k+1} + h_k\left(s^3 - s^2\right)m_{k+1} \quad (13)$$

where $s = (t - t_k)/(t_{k+1} - t_k)$ represents the locally normalized time variable ($0 \le s \le 1$) and $h_k = t_{k+1} - t_k$ is the time interval.

The derivation of this algorithm proceeds as follows. First, the secant slope between adjacent discrete forecast frames is determined by $\delta_k = (P_{k+1} - P_k)/(t_{k+1} - t_k)$. The initial tangent slope at internal nodes is then assigned as the arithmetic mean of these adjacent secant slopes, $m_k = (\delta_{k-1} + \delta_k)/2$. To prevent the generation of artificial extrema, an

absolute flatness constraint is applied: if $\delta_{k-1} \cdot \delta_k \leq 0$—indicating a local precipitation peak or a zero-rainfall period—the node tangent m_k is strictly set to zero. To guarantee strict monotonicity within the interval, the algorithm monitors the slope ratio parameters $\alpha_k = m_k/\delta_k$ and $\beta_k = m_{k+1}/\delta_k$. If the vector (α_k, β_k) falls outside the safe domain defined by $\alpha_k^2 + \beta_k^2 \leq 9$, a scaling factor $\tau_k = 3/\sqrt{\alpha_k^2 + \beta_k^2}$ is applied to correct the boundary tangent slopes via $m_k \leftarrow \tau_k \alpha_k \delta_k$ and $m_{k+1} \leftarrow \tau_k \beta_k \delta_k$.

The rainfall hyetograph reconstructed via this shape-preserving method remains non-negative and strictly retains the physical extrema of the original rainfall sequence. More importantly, it yields a temporally continuous source term $S_h(t)$ with a continuous first derivative, which is essential for stable hydrodynamic integration at second-level time steps. Consequently, this method mitigates the risk of numerical divergence associated with abrupt high-resolution forcing, providing a robust mathematical foundation for seamlessly coupling AI-based nowcasts with hydrodynamic simulations.

A sensitivity test was further conducted to compare various temporal treatments of the 6 min rainfall forcing, including stepwise input, linear interpolation, conventional cubic spline interpolation, and monotone PCHIP/Fritsch–Carlson interpolation. The results indicate that the stepwise input preserves the original rainfall amount but introduces abrupt source-term jumps at the 6 min boundaries. During high-intensity rainfall periods, such discontinuities significantly increase the nonlinear iteration burden of TELEMAC-2D and may cause the solver to exceed the preset maximum iteration count. While conventional cubic spline interpolation smooths the rainfall series, it may generate overshoot or negative rainfall values when rainfall intensity changes sharply. Linear interpolation avoids overshoot but remains merely piecewise linear. The monotone PCHIP/Fritsch–Carlson method, however, preserves non-negativity and local extrema while providing a continuous rainfall source term. Therefore, it was adopted as the coupling strategy in this study.

2.6. TELEMAC-2D Model Setup and Parameterization

2.6.1. Mesh Generation and Topographic Mapping

To accurately resolve the irregular planform of the river boundaries, complex floodplain macro-topography, and local linear drainage pathways, an unstructured triangular computational mesh was constructed (Figure 3). The final discretized domain comprises 9219 nodes and 18,112 triangular elements. Local mesh refinement was strategically enforced along the main Yangtze River channel and near critical hydrological control stations (Shishou and Jianli), while a coarser resolution was maintained in hydraulically insensitive peripheral zones. The spatial scales of the generated mesh were validated using two parallel geometric metrics: Edge Length Distribution, where the minimum, mean, and maximum triangular edge lengths are 86.53 m, 349.82 m, and 762.89 m, respectively; and Equivalent Side Length, with minimum, mean, and maximum equivalent side lengths of 111.38 m, 339.84 m, and 634.05 m, respectively. This variable-resolution mesh design ensures an optimal trade-off between local hydraulic fidelity and global computational efficiency.

2.6.2. Rainfall–Runoff and Friction Parameterization

Rainfall–runoff processes over the grid cells were simulated using the Soil Conservation Service Curve Number (SCS-CN) module integrated within TELEMAC-2D. Rather than using a lumped configuration, a spatially distributed CN field was generated by intersecting the 30 m China land-cover dataset with local soil type datasets. Standard SCS-CN lookup tables were used to map CN values onto each distinct soil–vegetation complex, which were then resampled onto the unstructured triangular mesh. In the steering configuration, the parameters were specified as follows:

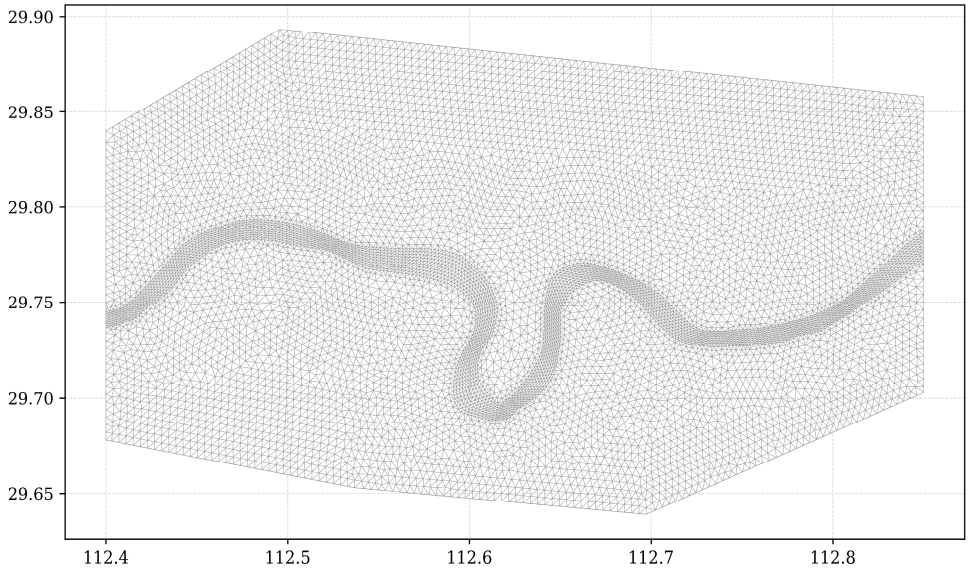


Figure 3. Unstructured mesh of the study area in the Jingjiang reach of the Yangtze River Basin.

RAINFALL–RUNOFF MODEL = 1
ANTECEDENT MOISTURE CONDITIONS = 2
The spatially distributed parameter was introduced via the private variable CN

Bottom friction coefficients were assigned based on land-use classes and bed materials in accordance with the *Hydraulic Calculation Manual* (2nd edition). Lower resistance fields were prescribed for the main channel and open waterbodies, whereas higher roughness was allocated to vegetated floodplains, croplands, and urban zones.

The model steering file specified LAW OF BOTTOM FRICTION = 3 with a reference baseline Strickler coefficient of 30 m^3/s (corresponding to a mean Manning's $n \approx 0.033\ s/m^3$, which was subsequently fine-tuned via calibration against observed gauge data.

2.6.3. Boundary and Initial Conditions

To ensure a mathematically well-posed and physically realistic simulation, rigorous boundary and initial conditions were prescribed for the TELEMAC-2D solver. At the upstream boundary located at Shishou station, a time-dependent prescribed discharge condition (liquid boundary with specified flow) was imposed. This continuous hourly Shishou discharge dataset was confidentially provided by Yangtze Ecology and Environment Co., Ltd. and remains non-public; its reliability and usability were rigorously verified and demonstrated through comprehensive cross-validation against publicly available observed water level records at the same station. Conversely, at the downstream outlet at Jianli station, a time-dependent prescribed water level boundary condition (liquid boundary with specified stage) was applied. All driving hydrological and meteorological records for the Jianli station are publicly available, and the corresponding event-level data excerpts have been fully provided in Appendix A.

The initial hydraulic state across the unstructured grid was established by interpolating observed water levels between the Shishou and Jianli stations to generate a steady-state initial flow field. To eliminate potential numerical transients, non-physical shocks, and mass-conservation oscillations induced by the initial state adjustment, a dedicated spin-up period was implemented for each flood event. The simulation workflow was purposefully initiated at T_{start}, allocating a spin-up duration of approximately 24 to 64 h prior to the critical storm onset time (T_0). This setup guaranteed that the hydrodynamic model achieved

a fully developed, numerically stable hydraulic baseline before the introduction of high-frequency dynamic rainfall forcing.

2.7. Evaluation Strategy and Forcing-Replacement Experiment

2.7.1. Meteorological Evaluation Design

To assess the performance of the precipitation nowcasting model Diff_ConvLSTM, forecasts from 0 to 3 h (2023–2024) are compared against radar observations over the region 111–115° E and 29–32° N. Delineation of the various precipitation regimes (e.g., light-to-moderate rainfall, and severe convection extremes) will be accomplished using thresholds of 20, 30, 35 and 40 dBZ.

Pixel-wise verification employs standard categorical metrics, including the Critical Success Index (CSI), Probability of Detection (POD), False Alarm Ratio (FAR), and Heidke Skill Score (HSS). To account for spatial displacement errors inherent in high-resolution forecasts, multi-scale pooling techniques are introduced. Specifically, CSI_{pool4} and CSI_{pool16} evaluate the forecast skill at spatial aggregation scales of 4 and 16, respectively. Relaxing the strict pixel-to-pixel matching constraint provides a more robust assessment of the model's ability to capture overarching mesoscale precipitation structures.

Besides categorical measures, we utilize Peak Signal-to-Noise Ratio (PSNR), Spatial Similarity Index Measure (SSIM), and Learned Perceptual Image Patch Similarity (LPIPS) to quantify the structural and perceptual fidelity of the predicted radar fields. Higher values of PSNR and SSIM reflect better pixel-level and structural similarity with the observations, while lower values of LPIPS indicate higher perceptual similarity in feature space, thus showcasing the model's ability to generate realistic convective textures.

2.7.2. Hydrological and Hydrodynamic Evaluation Design

A major challenge with coupled meteorological–hydrodynamic models is distinguishing rainfall-forcing errors from the inherent hydraulic ones. The full response of the system is not captured when the evaluation is restricted to only the 0–3 h rainfall window. In general, the time taken by basin routing is far greater than the time of the rainfall event and downstream flood peaks tend to occur many hours after the end of the rain. To overcome this limit, we develop a forcing-replacement experiment inside a deterministic hindcast framework. A forecast-observation splicing strategy helps to construct a continuous forcing sequence and extend the simulation window to the entire flood life cycle, which includes runoff generation, channel routing, and recession.

For the selected case study, the simulation period spanned from 08:00 on 27 June 2023 (T_{start}) to 14:00 on 2 July 2023 (T_{end}). Observations indicated a major rainfall system propagating from the upstream Shishou station toward the downstream Jianli station (Figure 4), with the most intense precipitation concentrated within a 3 h window beginning at 00:00 on 30 June. Thus, the onset time was designated the crucial start time (T_0). The following intervals (T_0 to $T_0 + 3$h) were selected as high-resolution coupling windows to examine how upstream–downstream rainfall heterogeneity affects the downstream flood response.

Four driving scenarios are formulated to systematically isolate the impact of different rainfall forcings. The first scenario (RAIN0) will be adopted as the reference case. This scenario does not have areal rainfall input. It has only upstream measured boundary flows. The aim of this reference case is to quantify rainfall contribution in terms of downstream flood volume. Scenario 2 (RAIN1) represents the reference hindcast scenario, wherein actual rain gauge observations are utilized as the continuous forcing field from T_{start} to T_{end}. Scenario 3 (RAIN2) simulates a conventional operational forecasting configuration; during the critical flood window (T_0 to $T_0 + 3$h), the model is driven by a spatially interpolated,

low-resolution (9 km, 3-hourly) ECMWF areal rainfall forecast, which is followed by a transition to gauge-based observations for the remainder of the simulation. Finally, Scenario 4 (RAIN3) constitutes the core experimental group evaluating the proposed high-resolution framework. In this scenario, the Diff_ConvLSTM-generated AI nowcasting fields (1 km, 6 min frequency) are applied to drive the model during the critical 0–3 h window, followed by a continuous transition to actual observational data until T_{end}. By comparing the discrepancies among RAIN2, RAIN3, and the RAIN1 benchmark, the extent to which early-stage (0–3 h) precipitation errors through the nonlinear hydrodynamic routing system, and their impact on the magnitude and timing of the flood peak, can be systematically assessed.

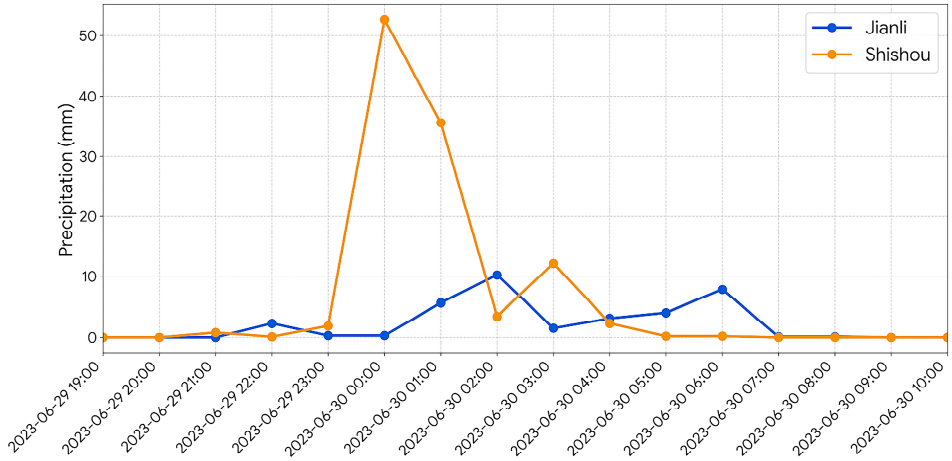


Figure 4. Rainfall time series at Shishou and Jianli meteorological stations.

To further examine the robustness of the forcing-replacement results, an additional rainfall–flood event from 08:00 on 21 June 2024 to 14:00 on 23 June 2024 was selected as an independent validation case. The same scenario configuration was applied to this event, including RAIN0 without areal rainfall input, RAIN1 driven by observed rainfall, RAIN2 driven by low-resolution forecast rainfall during the critical 0–3 h window, and RAIN3 driven by high-resolution AI-based nowcasting rainfall during the same window. This additional experiment was designed to evaluate whether the hydrodynamic benefits of high-resolution AI rainfall forcing were consistent across different flood events. The hydrological and hydrodynamic responses under varying rainfall forcings are evaluated using both station-based hydrograph metrics and spatial inundation metrics.

The hydrograph performance is quantified using the Nash–Sutcliffe Efficiency (NSE), coefficient of determination (R^2), Kling–Gupta Efficiency (KGE), Percent Bias (PBIAS), Relative Error of Peak Discharge (PRE), and Peak Timing Error (PTE). These metrics collectively assess overall goodness-of-fit, trend consistency, volumetric bias, and flood-peak magnitude and timing. Additionally, the spatial inundation response is evaluated relative to the observation-driven RAIN1 reference scenario using inundated area difference, mean depth difference, depth RMSE, Intersection over Union (IoU), F1-score, and Cohen's Kappa coefficient. These spatial metrics quantify differences in flood extent, water-depth distribution, and inundation-pattern agreement.

3. Results

3.1. Performance of Precipitation Nowcasting

To quantitatively evaluate the performance of the proposed nowcasting model, comparative analyses are conducted across the thresholds on the validation dataset. The primary evaluation metrics and their corresponding relative improvement rates are sum-

marized in Tables 1–3. Compared to the benchmark model, Diff_ConvLSTM exhibits substantial enhancements. Specifically, the Critical Success Index (CSI) at the 20 dBZ threshold increases by 19.13%, while the Probability of Detection (POD) at the 30 dBZ threshold improves by 28.70% (Table 1), indicating that residual diffusion effectively rectifies the "high-value attenuation" issue prevalent in ConvLSTM. Furthermore, under extreme thresholds, Diff_ConvLSTM achieves a remarkable 40.06% increase in POD and a 15.14% improvement in CSI at 35 dBZ, alongside a 65.80% surge in POD and a 2.25% improvement in CSI at 40 dBZ (Table 2).

Table 1. Verification results of different models at the 20 and 30 dBZ thresholds and their relative improvements over the baseline model.

Model	20 dBZ Threshold			30 dBZ Threshold		
	CSI↑	POD↑	HSS↑	CSI↑	POD↑	HSS↑
ConvLSTM	0.3722	0.4922	0.5045	0.2563	0.3293	0.3874
Diff_ConvLSTM	0.4434	0.5124	0.5865	0.2968	0.4238	0.4360
	19.13%	**4.10%**	**16.25%**	**15.80%**	**28.70%**	**12.55%**

Note: Bold values indicate the best results. Relative improvement (%) denotes the percentage change in Diff_ConvLSTM relative to ConvLSTM.

Table 2. Verification results of different models at the 35 and 40 dBZ thresholds and their relative improvements over the baseline model.

Model	35 dBZ Threshold			40 dBZ Threshold		
	CSI↑	POD↑	HSS↑	CSI↑	POD↑	HSS↑
ConvLSTM	0.2041	0.2601	0.3237	0.1555	0.1760	0.2529
Diff_ConvLSTM	0.2350	0.3643	0.3601	0.1590	0.2918	0.2569
	15.14%	**40.06%**	**11.24%**	**2.25%**	**65.80%**	**1.58%**

Note: Bold values indicate the best results. Relative improvement (%) denotes the percentage change in Diff_ConvLSTM relative to ConvLSTM.

Table 3. Mean verification results of different models and their relative improvements over the baseline model.

Model	CSI↑	CSIpool4↑	CSIpool16↑	PSNR↑	SSIM↑	LPIPS↓
ConvLSTM	0.2470	0.2514	0.2616	27.97	0.700	0.305
Diff_ConvLSTM	0.2835	0.3562	0.5114	24.86	0.693	0.169
	14.78%	**41.69%**	**95.49%**	−11.12%	−1.00%	**−44.59%**

Note: Bold values indicate the best results. Relative improvement (%) denotes the percentage change in Diff_ConvLSTM relative to ConvLSTM. Negative values indicate a decrease in the metric value; for LPIPS, this corresponds to an improvement in perceptual similarity.

In terms of average metrics presented in Table 3, the multi-scale pooling CSIs (CSI_{pool4} and CSI_{pool16}) for Diff_ConvLSTM increase by 41.69% and 95.49%, respectively, indicating a substantial improvement in preservation of rainband morphology. LPIPS of Diff_ConvLSTM scheme drops by 44.59%, while SSIM remains the same in terms of perceptual quality. On the contrary, the PSNR drops mildly (−11.12%). This decline is presumably due to a common trade-off in diffusion-based models where enhancing perceptual realism comes at the cost of greater pixel-level error, largely due to noise made during the diffusion training.

When the reflectivity thresholds are set higher (≥35 dBZ), the Diff_ConvLSTM shows a distinct advantage in detecting rainfall intensity with a POD gain of 20–66%. As indicated by these results, forecasting the missed-convective core problem with conventional ConvLSTM is alleviated with the introduction of the residual diffusion module.

3.2. Calibration and Applicability of the TELEMAC-2D Model

Before undertaking the Meteorological Forcing Field Replacement Experiment, it is necessary to verify the physical reliability of the hydrodynamic model. For this purpose, continuous discharge observations at key hydrological stations of the area of study have been utilized for long-term calibration and validation of high-resolution TELEMAC-2D model.

As shown in Figure 5, the results of the continuous simulation yield simulated discharge (red line) and observed discharge (black line), showing a good match, which implies high model fidelity. Over the course of annual hydrograph evolution, the model satisfactorily reproduces the nonlinear hydraulic characteristic in rising and falling limbs This includes the mild fluctuations in baseflow that occur during the dry season (approximately 6000–7000 m^3/s) and the peaks of multiple flooding due to heavy rain in the flood season, especially the extreme peak discharge which exceeds 20,000 m^3/s in October.

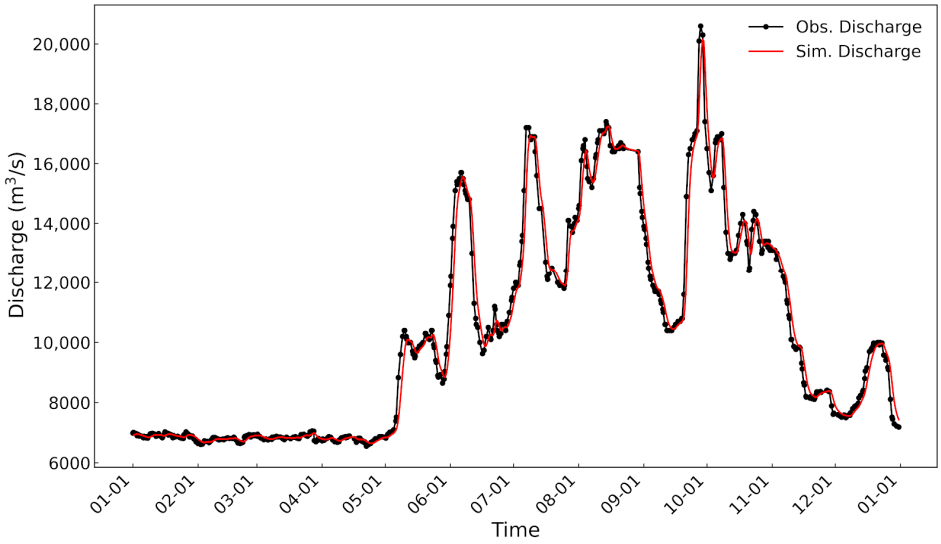


Figure 5. Comparison of observed (black line) and simulated (red line) discharge time series in the study area in 2023 (black line: observed discharge; red line: simulated discharge).

To complement visual inspection, an extended diagnostic evaluation was conducted, as summarized in Table 4. The coefficient of determination (R^2 = 0.9793) indicates a strong linear consistency between the simulated and observed annual hydrographs. The RMSE and MAE are 501.32 m^3/s and 295.48 m^3/s, respectively, suggesting that the absolute discharge error remains moderate relative to the magnitude of the annual flow variations. Although the model reproduces the overall hydrograph shape and peak magnitude reasonably well, the diagnostic metrics reveal a clear timing limitation. The peak-discharge absolute error (PDAE) is 455.44 m^3/s, corresponding to the difference between the observed peak discharge of 20,600 m^3/s and the simulated peak discharge of 20,144.56 m^3/s. However, the Peak Timing Error (PTE) reaches +8 h, indicating that the simulated flood peak occurs later than the observed peak. A cross-correlation analysis further shows that the maximum correlation coefficient of 0.9992 is obtained when the simulated discharge series is shifted by approximately +9 h. This confirms that the main discrepancy is associated with phase lag rather than a failure in reproducing the hydrograph shape or flood volume.

To further assess the performance of the numerical model in reproducing the temporal discharge dynamics, a linear regression analysis comparing the observed and simulated discharge values was conducted (Figure 6). A total of 562 discharge sample points were used for the calibration and validation analysis during the 2023 simulation period. The dispersion graphic demonstrates a high degree of agreement, with the data points tightly clustered along the 1:1 reference line. The fitted linear regression equation is $y = 0.9806x + 195.85$,

yielding a coefficient of determination (R^2) of 0.9793. According to the widely adopted hydrological model evaluation guidelines proposed by Moriasi et al. [44], a streamflow simulation is classified as "very good" when NSE > 0.75, R^2 > 0.75, and PBIAS < ±10%. The calculated diagnostic metrics for this long-term continuous simulation (NSE = 0.97, R^2 = 0.97, and PBIAS = −0.02%) comfortably exceed these stringent thresholds. This confirms that the model achieves high fidelity and avoids significant systematic overestimation or underestimation across both low and peak flow conditions.

Table 4. Extended diagnostic evaluation metrics for the long-term TELEMAC-2D simulation in 2023.

Evaluation Metric	Value
NSE	0.97
R^2	0.97
RMSE	501.32 m^3/s
MAE	295.48 m^3/s
PDAE	455.44 m^3/s
KGE	0.98
PBIAS	−0.02%
PRE	−2.21%
PTE	~8 h
Cross-corr lag	~9 h
Rising-limb RMSE	549.11 m^3/s
Variance ratio α	0.9910

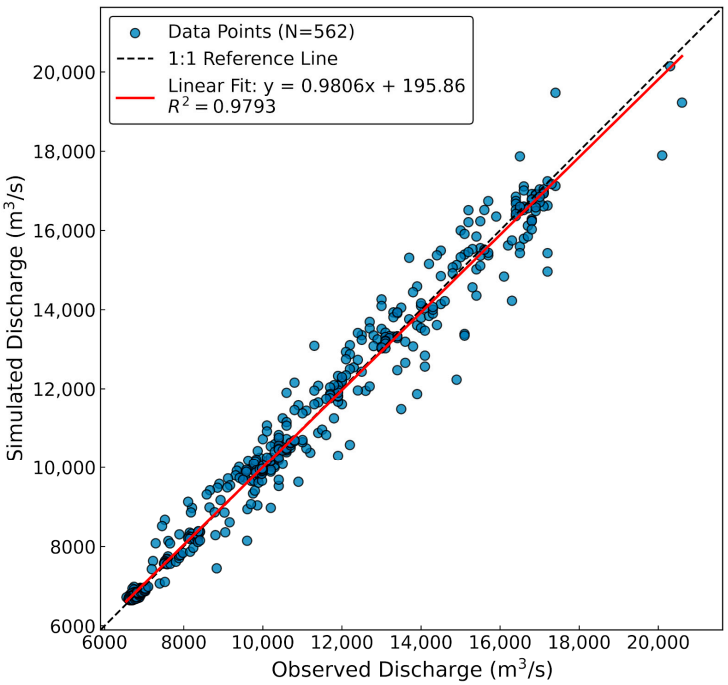


Figure 6. Scatter plot and linear regression analysis of observed versus simulated discharge for the TELEMAC-2D model calibration.

The rising-limb RMSE is 549.11 m^3/s, which is higher than the overall RMSE of 501.32 m^3/s, indicating that the rapid flood-wave rising stage is more difficult to reproduce than the full hydrograph. Meanwhile, the variance ratio α is 0.9910, suggesting that the model preserves the observed variability magnitude without excessive numerical smoothing. Overall, these results demonstrate that the TELEMAC-2D model is suitable for reproducing the main discharge evolution and peak magnitude, while also highlighting the remaining uncertainty in flood-wave propagation timing.

3.3. Hydrodynamic Response During the 2023 Event

The simulated evolution of streamflow at the Jianli station, covering the period from 00:00 on 30 June 2023 to 14:00 on 2 July 2023, is illustrated in Figure 7. To quantitatively assess the hydrodynamic response to varying rainfall forcings, the statistical performance metrics for each simulation scenario are summarized in Table 5. In the RAIN0 scenario, which relies solely on upstream boundary inflows without any areal rainfall input, the simulated discharge demonstrates a relatively smooth and attenuated variation. This scenario is used as a reference for the subsequent ones and it allows for a clear assessment of the impact of areal rainfall forcing on flood-peak development.

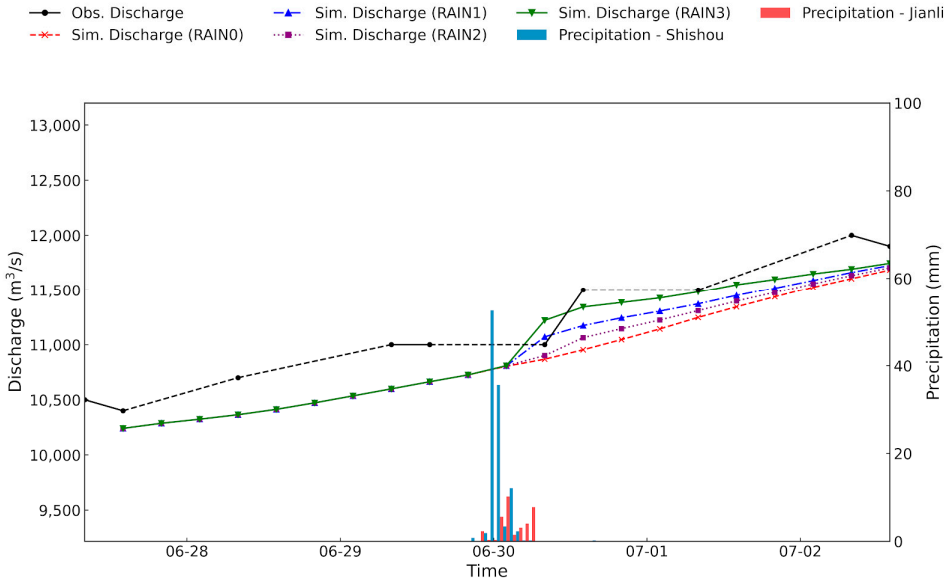


Figure 7. The simulated streamflow at Jianli station from 00:00 on 30 June 2023 to 14:00 on 2 July 2023.

Table 5. Evaluation metrics of the simulated results under different rainfall-forcing scenarios.

Scenario	NSE	R^2	KGE	PBIAS	PRE	PTE
RAIN0	0.5697	0.9401	0.9375	−2.75%	−2.63%	~6 h
RAIN1	0.7034	0.9246	0.9534	−2.11%	−2.29%	~6 h
RAIN2	0.6445	**0.9502**	**0.9600**	−2.50%	−2.46%	~6 h
RAIN3	**0.7383**	0.8869	0.9042	**−1.64%**	**−2.13%**	~6 h

Note: Bold values indicate the best performance for each metric. For PBIAS and PRE, values closer to zero indicate better performance.

Under the RAIN1 scenario, the application of observed station-based rainfall forcing allows the model to successfully reproduce the initial flood peak at 08:00 on 30 June. However, the spatial interpolation of gauge data inevitably smooths localized precipitation extremes, thereby weakening runoff concentration across the complex floodplain terrain. Conversely, during the critical 0–3 h window, RAIN2 is driven by low-resolution forecast forcing, which exacerbates this spatial averaging effect and leads to a pronounced attenuation of the localized intense rainfall signal. Consequently, the initial flood peak is not fully developed. Quantitative metrics in Table 5 indicate that, compared to RAIN1, RAIN2 exhibits a Relative PRE of approximately −2.46% and an overall volumetric bias (PBIAS) of −2.50%

In the RAIN3 scenario, the high-resolution forecast is seamlessly coupled to the hydrodynamic model via monotonic shape-preserving interpolation. This preserves localized extreme rainfall intensities, thereby enhancing the representation of infiltration-excess

runoff during the early-stage response. As a result, the peak-discharge underestimation (PRE) is reduced to −2.13% and the overall volumetric bias (PBIAS) improves to −1.64%.

In terms of spatial distribution, the different forcing scenarios exhibit noticeable differences in channel and floodplain water depths (Figure 8). To better distinguish the hydrodynamic responses in different hydraulic zones, Figure 8 separately presents the enlarged main-channel water-depth distributions and the corresponding floodplain inundation-depth distributions. RAIN0 (Figure 8a1,a2), relying solely on channel routing, shows lower water depths within the main channel and negligible floodplain inundation. In contrast, RAIN1 (Figure 8b1,b2), driven by gauge-based rainfall, displays significant water-depth expansion in the floodplains flanking the main channel. In RAIN2 (Figure 8c1,c2), the spatial averaging inherent in the coarse-resolution ECMWF forecast smooths high-intensity rainfall, resulting in fragmented and spatially underestimated floodplain inundation. Conversely, RAIN3 (Figure 8d1,d2) utilizes the 1 km, 6 min high-frequency AI-based nowcasting, where localized intense rainfall effectively triggers infiltration-excess runoff across the river network and micro-topography. The floodplain water-depth distribution in RAIN3 exhibits enhanced spatial agreement compared with RAIN2 and is closer to the observation-driven RAIN1 reference in spatial overlap metrics, although it simultaneously retains localized high-value features that contribute to a regional over-amplification.

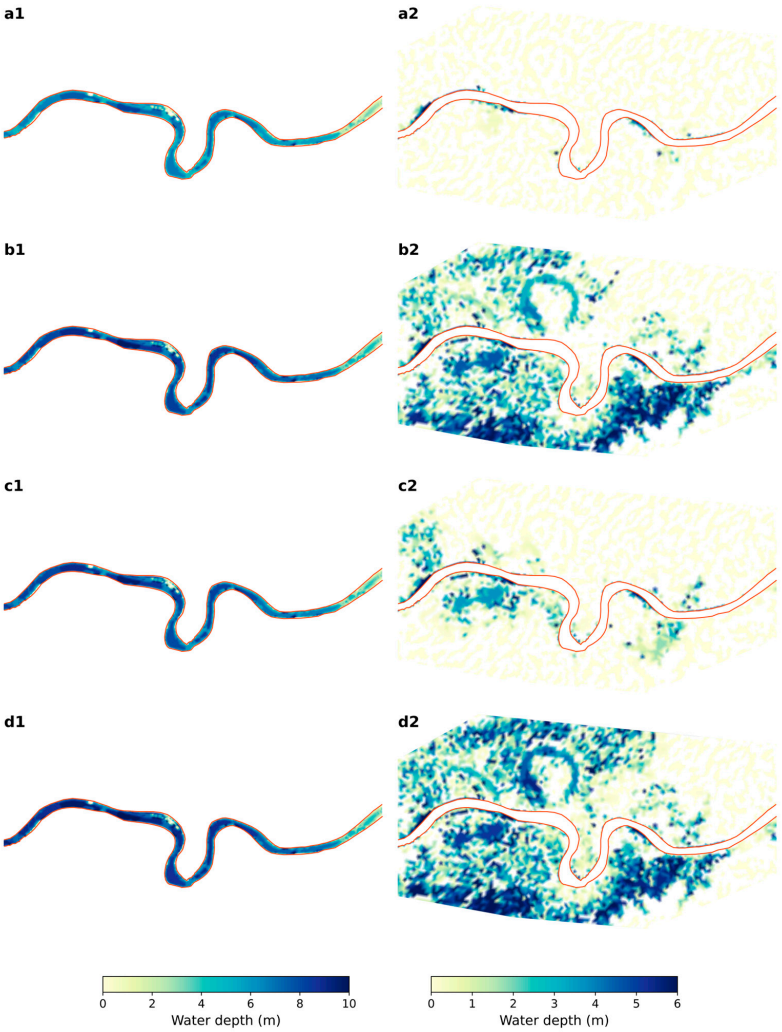


Figure 8. Spatial distribution of simulated water depth under different rainfall-forcing scenarios: (**a1**,**a2**) RAIN0, (**b1**,**b2**) RAIN1, (**c1**,**c2**) RAIN2, and (**d1**,**d2**) RAIN3. Panels (**a1**–**d1**) show the enlarged main-channel water depth, while panels (**a2**–**d2**) show the corresponding floodplain inundation depth. Separate color scales are used for the channel and floodplain panels.

To further quantify the spatial differences shown in Figure 8, spatial inundation metrics were calculated using RAIN1 as the observation-driven reference scenario (Table 6). Compared with RAIN1, RAIN2 substantially underestimates both the inundation extent and water depth. The inundated area is reduced by 61.14%, and the mean water-depth difference reaches −1.50 m. The depth RMSE is 2.24 m, while the IoU and F1-score are only 0.274 and 0.430, respectively, indicating a weak spatial overlap with the RAIN1 reference.

Table 6. Spatial inundation metrics relative to the observation-driven RAIN1 reference.

Scenario	Inundated Area Difference (%)	Mean Depth Difference (m)	Depth RMSE (m)	IoU	F1-Score	Kappa
RAIN2 − RAIN1	−61.14	−1.50	2.24	0.274	0.430	0.369
RAIN3 − RAIN1	+62.20	+1.01	1.44	0.556	0.715	0.637

In contrast, RAIN3 shows a much higher spatial consistency with RAIN1. Although RAIN3 overestimates the inundated area by 62.20% and produces a positive mean depth difference of 1.01 m, its depth RMSE decreases to 1.44 m. In addition, the IoU, F1-score, and Kappa increase to 0.556, 0.715, and 0.637, respectively. These results indicate that the high-resolution AI-based rainfall forcing improves the spatial agreement of inundation patterns relative to the low-resolution RAIN2 forcing. However, the positive area and mean-depth biases explicitly demonstrate that RAIN3 exhibits a systematic over-amplification of the inundation response relative to the RAIN1 benchmark.

Because the 2023 event represents only one hydrodynamic response case, an additional 2024 rainfall–flood event was further examined to assess whether the forcing-replacement results are robust across different flood conditions.

3.4. Independent Hydrodynamic Evaluation During the 2024 Event

To further evaluate the robustness of the proposed forcing-replacement framework, an additional rainfall–flood event from 08:00 on 21 June 2024 to 14:00 on 23 June 2024 was examined. As shown in Figure 9, the observed discharge at Jianli station increased from approximately 16,500 m^3/s to a peak of about 17,800 m^3/s, indicating a clear flood response associated with the rainfall process over the Shishou–Jianli reach. The rainfall observations show that the main rainfall period occurred around 22 June, with intense precipitation first observed near Shishou and subsequently affecting Jianli.

The four rainfall-forcing scenarios produced clearly different hydrodynamic responses, as quantitatively summarized in Table 7. RAIN0, which excludes areal rainfall input, substantially underestimated the rising limb and yielded the weakest simulation performance, with an NSE of −1.0539. RAIN2, driven by low-resolution forecast rainfall during the critical window, also failed to fully reproduce the observed discharge evolution, resulting in a negative NSE of −0.3157 and a PBIAS of −2.05%. In contrast, RAIN1, driven by observed rainfall, reproduced the overall hydrograph reasonably well, with an NSE of 0.7067 and an R^2 of 0.8665.

The RAIN3 scenario, which used high-resolution AI-based nowcasting rainfall forcing during the critical 0–3 h window, provided the best overall performance for this event. Compared with RAIN2, RAIN3 increased the NSE from −0.3157 to 0.8043 and the R^2 from 0.5769 to 0.8962. The volumetric bias was also substantially reduced, with PBIAS improving from −2.05% to −0.33%. In terms of peak discharge, the PRE decreased from −1.70% in RAIN2 to −0.42% in RAIN3, indicating that the high-resolution AI rainfall forcing better captured the rainfall contribution to flood-peak formation. However, the PTE remained approximately 5–6 h across the scenarios, indicating that the improvement was mainly reflected in discharge magnitude and volume rather than peak timing.

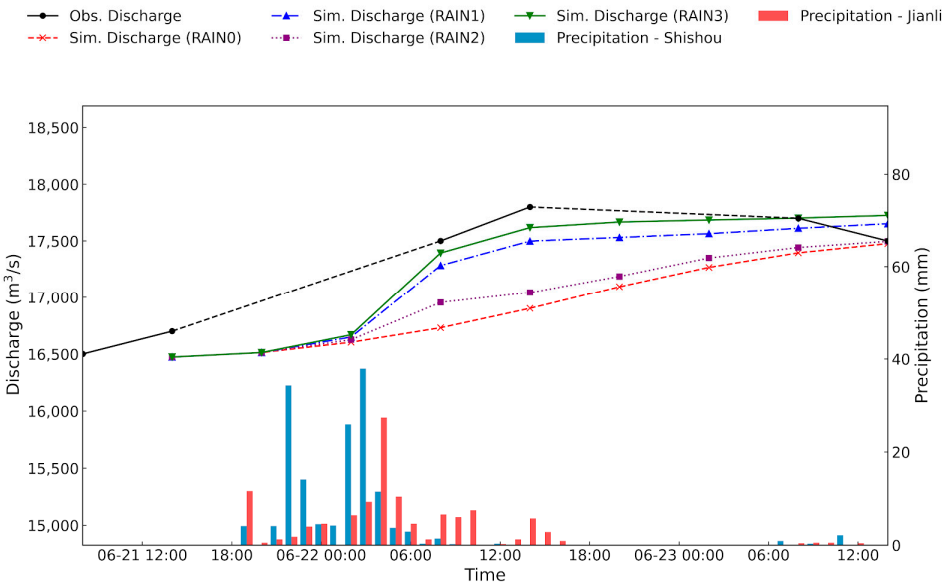


Figure 9. Simulated and observed discharge at Jianli station under different rainfall-forcing scenarios during the 21–23 June 2024 event. Blue and red bars indicate hourly precipitation at Shishou and Jianli stations, respectively; lines indicate observed and simulated discharge series.

Table 7. Evaluation metrics of the simulated results under different rainfall-forcing scenarios during the 21–23 June 2024 event.

Scenario	NSE	R^2	KGE	PBIAS	PRE	PTE
RAIN0	−1.0539	0.3944	0.6271	−2.55%	−1.81%	~6 h
RAIN1	0.7067	0.8665	**0.8604**	−0.78%	−0.83%	~5 h
RAIN2	−0.3157	0.5769	0.7551	−2.05%	−1.70%	~6 h
RAIN3	**0.8043**	**0.8962**	0.7825	**−0.33%**	**−0.42%**	~5 h

Note: Bold values indicate the best performance for each metric. For PBIAS and PRE, values closer to zero indicate better performance.

These results are consistent with the 2023 event and further support the hydrodynamic value of high-resolution AI-based rainfall forcing. Nevertheless, the KGE of RAIN3 was lower than that of RAIN1, indicating that the advantage of RAIN3 was not uniform across all metrics. Therefore, the additional 2024 event reinforces the conclusion that AI-based nowcasting improves selected hydrodynamically relevant aspects, particularly flood-volume bias and peak-discharge magnitude, while the improvement in timing-related metrics remains limited. Spatially, similar to the 2023 event, the high-resolution driving configuration yields an inundation pattern closer to the observation-driven reference than the low-resolution forecast in terms of spatial overlap, despite maintaining a notable positive bias in both inundated area and local water depth.

4. Discussion

4.1. Result Analysis

The results indicate that the spatial and temporal resolution of rainfall forcing during the initial 0–3 h window exerts a strong influence not only on the early runoff-generation process but also on the subsequent hydrograph evolution. The contrast between RAIN2 and RAIN3 suggests that higher-resolution rainfall forcing is more effective in capturing localized intense precipitation and its associated early-stage hydrodynamic response. In the present case, this improvement is reflected in higher NSE values, reduced PBIAS, and lower PRE under RAIN3 relative to RAIN2. These findings suggest that the AI-based

high-resolution nowcasting provides a more physically consistent representation of the rainfall structures relevant to flood generation in low-relief floodplain environments.

The contrast between RAIN2 and RAIN3 aligns with prior research highlighting the hydrological significance of spatiotemporal variability in rainfall. When rainfall forcing is spatially or temporally smoothed, localized high-intensity cores may be diminished, leading to a reduction in runoff concentration and a delay or attenuation of the flood response. This mechanism has been documented in earlier numerical experiments concerning rainfall variability and basin flood response [18], as well as in extensive flash-flood studies that demonstrate how the spatial organization of rainfall significantly influences flood severity [19]. The current findings extend these insights to an AI-nowcasting-driven rain-on-grid hydrodynamic framework, illustrating that high-resolution rainfall structures can enhance critical hydrodynamic aspects, including peak-discharge magnitude, volumetric consistency, and spatial inundation agreement.

The spatial inundation metrics further support this interpretation. RAIN3 enhances the spatial overlap of inundated areas and reduces the root mean square error (RMSE) of depth compared to RAIN2, confirming that high-resolution AI-based rainfall forcing achieves closer alignment with the observation-driven RAIN1 reference in spatial overlap metrics than its low-resolution counterpart. However, the positive biases in inundated area and mean depth explicitly indicate a significant over-amplification of the modeled inundation process, underscoring the critical need for further joint calibration of small-scale rainfall intensity, grid-scale infiltration parameters, and floodplain roughness.

The additional 2024 validation event provides further evidence for this interpretation. In this event, RAIN3 outperformed RAIN2 in terms of NSE, R^2, PBIAS, and PRE, indicating that high-resolution AI-based rainfall forcing enhances both the magnitude and volumetric representation of the flood response. Notably, the reduction in PBIAS from −2.05% to −0.33% and PRE from −1.70% to −0.42% suggests that the nowcasting-based rainfall forcing better preserves the hydrologically effective rainfall signal during the early stages of the event. However, the unchanged PTE and the lower KGE compared to RAIN1 confirm that the advantages of RAIN3 should not be interpreted as uniform improvements across all metrics. Instead, the two-event comparison indicates that the primary contribution of high-resolution AI rainfall forcing lies in enhancing discharge magnitude, flood-volume consistency, and hydrodynamically relevant rainfall structure.

One plausible explanation for the metric inconsistency is that high-resolution rainfall forcing enhances localized extremes and sharp gradients, which are important for reproducing flood peaks and floodplain inundation, but may also introduce stronger short-term fluctuations into the simulated hydrograph. As a result, improvements in peak magnitude and volumetric bias do not necessarily translate into higher correlation-based or variance-sensitive indices such as R^2 and KGE. In other words, the higher-resolution forcing appears to preferentially improve the simulation of hydrologically critical extremes rather than uniformly optimizing all aspects of the full discharge time series. This interpretation is consistent with the spatial results, where RAIN3 produces inundation-depth patterns closer to the observation-driven reference than RAIN2.

4.2. Innovation

From a methodological perspective, the added value of high-resolution precipitation nowcasting is reflected not only in improved conventional meteorological skills, but more importantly in its potential hydrodynamic relevance after coupling with flood-routing models. The forcing-replacement design provides a practical way to isolate the propagation of early-stage rainfall errors through the nonlinear flood-routing system. This is particularly

important because the main hydrodynamic consequences of rainfall errors may emerge several hours after the rainfall event itself, rather than within the nowcasting window alone.

The results also highlight the importance of stable temporal coupling between rainfall forcing and hydrodynamic integration. In this framework, the monotone shape-preserving interpolation serves as a numerical bridge between 6 min rainfall updates and second-scale hydrodynamic time stepping. This treatment reduces the risk of spurious oscillations while retaining the temporal structure of the forecast signal. Therefore, the contribution of the framework is not limited to the use of AI nowcasting itself, but also includes the construction of a numerically stable coupling pathway for rain-on-grid hydrodynamic simulation.

4.3. Limitations

Several limitations should be acknowledged. First, although two rainfall–flood events were examined, the hydrodynamic evaluation is still based on a limited number of cases rather than a large multi-event sample. Therefore, the results should be interpreted as a mechanism-based demonstration supported by two event-scale experiments, whereas the meteorological performance is evaluated over the broader 2023–2024 radar dataset.

Second, the present framework is mainly designed for short-duration convective rainfall events. Its added value may be weakened for long-duration stratiform precipitation events, in which rainfall structure is more spatially stable and less dependent on high-frequency convective evolution.

Third, uncertainties remain in radar-based rainfall estimation, infiltration parameterization, terrain representation, and hydrodynamic model configuration. These factors may affect different evaluation metrics in distinct ways, particularly those sensitive to peak magnitude and temporal variability. Future work should therefore extend the analysis to multiple flood events, a wider range of basin characteristics, and longer forecast lead times. Further investigation is also needed to quantify the interaction between high-resolution rainfall forcing and hydrodynamic parameter uncertainty in operational settings.

5. Conclusions

This study developed a flood-evolution forecasting framework that couples diffusion-enhanced precipitation nowcasting with the TELEMAC-2D hydrodynamic model. Using the Shishou–Jianli reach of the middle Yangtze River and its surrounding floodplain as a case study, the framework integrated 1 km, 6 min, 0–3 h rainfall forecasts from Diff_ConvLSTM into the rain-on-grid hydrodynamic simulation. A monotone shape-preserving piecewise cubic Hermite interpolation method was introduced to ensure stable temporal coupling between high-frequency rainfall forcing and second-scale hydrodynamic integration.

The main findings of this study are summarized as follows:

(1) Diff_ConvLSTM improved the representation of intense rainfall structures relative to the ConvLSTM baseline, particularly for localized high-value precipitation features relevant to flood generation. These improvements provided a more suitable rainfall-forcing field for hydrodynamic simulation.

(2) In the forcing-replacement experiment, the high-resolution AI-based rainfall forcing (RAIN3) outperforms the low-resolution forecast forcing (RAIN2) in several key hydrodynamic metrics, including NSE, PBIAS, and PRE. It also produced inundation-depth patterns that were more consistent with the observation-driven reference. These results indicate that higher-resolution rainfall forcing improves peak-discharge magnitude and spatial flood-response realism in this case.

(3) The advantage of RAIN3 was not uniform across all evaluation criteria. In the 2023 event, RAIN3 improved NSE, PBIAS, PRE, and inundation-pattern agreement relative to RAIN2, but its correlation- and variability-related metrics were not consistently

superior. In the 2024 validation event, RAIN3 further improved discharge magnitude and volumetric bias, whereas the peak-timing error remained unchanged. These results indicate that RAIN3 provides partial but hydrodynamically meaningful improvements rather than comprehensive superiority across all flood-process metrics.

(4) The proposed coupling framework provides an operationally relevant pathway for linking AI-based nowcasting with two-dimensional flood hydraulics. Its main contribution lies in combining high-resolution rainfall prediction, numerically stable temporal interpolation, and an end-to-end forcing-replacement design for diagnosing the downstream impact of early rainfall errors.

Overall, the two-event evaluation suggests that high-resolution AI-based nowcasting rainfall forcing can improve selected hydrodynamically important aspects of flood simulation, especially peak-discharge magnitude and flood-volume consistency. However, its benefits are not uniform across all metrics, and further multi-event evaluation is still required.

Author Contributions: Conceptualization, D.F. and J.Z.; methodology, D.F. and S.H.; software, D.F. and Y.D.; validation, D.F., S.H. and L.Z.; formal analysis, D.F. and Y.D.; investigation, S.H. and L.Z.; resources, J.Z.; data curation, Y.D. and L.Z.; writing—original draft preparation, D.F.; writing—review and editing, S.H. and J.Z.; visualization, D.F. and Y.D.; supervision, J.Z.; project administration, D.F. and J.Z.; funding acquisition, J.Z. All authors have read and agreed to the published version of the manuscript.

Funding: This research was funded by the Heavy Rainfall Research Foundation of China (BYKJ2025Q20), the Shaanxi Provincial Natural Science Basic Research Program (2024JC-YBQN-0290), the Major Science and Technology Project of the Ministry of Water Resources (SKS-2022014), and the Scientific Research Project of Yangtze Ecology and Environment Co., Ltd. (HBZB2024029).

Data Availability Statement: The data supporting the findings of this study are partially publicly available and partially restricted. Publicly available datasets include the ALOS World 3D–30 m (AW3D30 V4.1) terrain data (https://www.eorc.jaxa.jp/ALOS/en/dataset/aw3d30/aw3d30_e.htm, accessed on 11 April 2026), the annual 30 m China land-cover dataset (https://zenodo.org/records/15853565, accessed on 11 April 2026), and the National Basic Meteorological Element Dataset Product V3.0 of the China Meteorological Administration (http://www.nmic.cn/, accessed on 11 April 2026). The hydrological observation data and reservoir operation data were provided by Yangtze Ecology and Environment Co., Ltd. and are restricted in order to comply with confidentiality obligations of the Changjiang Water Resources Commission. The radar reflectivity composite data were provided by the China Meteorological Administration and are subject to data access restrictions and proprietary protection.

Acknowledgments: The authors would like to thank the data-providing agencies for supporting this study through the provision of hydrological, reservoir operation, and radar datasets. The authors also acknowledge the technical support related to data preparation and model implementation.

Conflicts of Interest: Author Jun Zhang was employed by Yangtze Ecology and Environment Co., Ltd. The remaining authors declare that the research was conducted in the absence of any commercial or financial relationships that could be construed as potential conflicts of interest.

Abbreviations

The following abbreviations are used in this manuscript:

NWP	Numerical Weather Prediction
ECMWF	European Centre for Medium-Range Weather Forecasts
DEM	Digital Elevation Model
AW3D30	ALOS World 3D–30 m
ConvLSTM	Convolutional Long Short-Term Memory

GTUNet	Global Temporal U-Net
MSE	Mean Squared Error
PSNR	Peak Signal-to-Noise Ratio
SSIM	Structural Similarity Index Measure
LPIPS	Learned Perceptual Image Patch Similarity
TELEMAC-2D	Two-Dimensional TELEMAC Hydrodynamic Model
SWEs	Shallow-Water Equations
CFL	Courant–Friedrichs–Lewy
PCHIP	Piecewise Cubic Hermite Interpolating Polynomial
SCS-CN	Soil Conservation Service Curve Number
CN	Curve Number
CSI	Critical Success Index
FAR	False Alarm Ratio
POD	Probability of Detection
HSS	Heidke Skill Score
NSE	Nash–Sutcliffe Efficiency
R^2	Coefficient of Determination
KGE	Kling–Gupta Efficiency
PBIAS	Percent Bias
PRE	Relative Error of Peak Discharge
PTE	Peak Timing Error
RMSE	Root Mean Square Error
MAE	Mean Absolute Error
PDAE	Peak-Discharge Absolute Error
IoU	Intersection over Union
F1-score	F1-score
Kappa	Cohen's Kappa Coefficient

Appendix A. Public Observational Data and Event-Selection Criteria

Appendix A.1. Event-Selection Criteria

To support transparency and reproducibility, this appendix provides the event-selection criteria and the publicly available observed rainfall and hydrological data used for the two selected rainfall–flood events. The events were selected according to two criteria.

First, the upstream Shishou station was required to record rainfall intensity greater than or equal to 10 mm h^{-1} for at least two consecutive hours, followed by rainfall at the downstream Jianli station. This criterion was used to identify rainfall systems propagating from Shishou toward Jianli. Second, at least one of the two stations was required to record rainfall intensity exceeding 20 mm h^{-1}. Such short-duration and high-intensity rainfall is difficult to capture accurately and is therefore suitable for evaluating the potential contribution of AI-based precipitation nowcasting.

Based on these criteria, only two rainfall–flood events were selected: the event from 00:00 on 30 June 2023 to 14:00 on 2 July 2023, and the event from 08:00 on 21 June 2024 to 14:00 on 23 June 2024. The corresponding rainfall, water-level, and discharge observations are listed in Tables A1–A4.

Appendix A.2. Observed Rainfall Data for the Two Selected Events

Table A1. Hourly observed rainfall at Shishou and Jianli stations during the 30 June 2023 event.

Time	Shishou Rainfall (mm)	Jianli Rainfall (mm)
30 June 202300:00:00	**52.6**	**0.3**
30 June 202301:00:00	**35.6**	**5.6**
30 June 202302:00:00	**3.4**	**10.2**

Table A1. *Cont.*

Time	Shishou Rainfall (mm)	Jianli Rainfall (mm)
30 June 2023 03:00:00	12.1	1.5
30 June 202304:00:00	2.3	3.1
30 June 2023 05:00:00	1.2	0.4
30 June 202306:00:00	0.5	0

Note: Bold rows indicate the critical 0–3 h nowcasting window simulated using meteorological-model rainfall forcing in this study.

Table A2. Hourly observed rainfall at Shishou and Jianli stations during the 21–23 June 2024 event.

Time	Shishou Rainfall (mm)	Jianli Rainfall (mm)
22 June 2024 00:00:00	12.5	4.2
22 June 2024 01:00:00	**18.3**	**10.5**
22 June 2024 02:00:00	**45.2**	**25.6**
22 June 2024 03:00:00	**32.1**	**30.4**
22 June 2024 04:00:00	15.6	18.2
22 June 2024 05:00:00	8.4	12.0
22 June 2024 06:00:00	4.2	8.5
22 June 2024 07:00:00	2.1	4.3
22 June 2024 08:00:00	1.0	2.1
22 June 2024 09:00:00	0.5	1.0

Note: Bold rows indicate the critical 0–3 h nowcasting window simulated using meteorological-model rainfall forcing in this study.

Appendix A.3. Observed Water-Level and Discharge Data for the Two Selected

Table A3. Observed water level and discharge at Shishou and Jianli hydrological stations during the 30 June–2 July 2023 event.

Time	Shishou		Jianli	
	Water Level (m)	Discharge (m^3 s^{-1})	Water Level (m)	Discharge (m^3 s^{-1})
30 June 2023 08:00:00	30.18	N/A	28.57	11,400
30 June 2023 14:00:00	30.22	N/A	28.6	11,500
01 July 2023 08:00:00	30.29	N/A	28.58	11,800
02 July 2023 08:00:00	30.28	N/A	28.51	12,000
02 July 2023 14:00:00	30.29	N/A	28.51	11,900

Table A4. Observed water level and discharge at Shishou and Jianli hydrological stations during the 21–23 June 2024 event.

Time	Shishou		Jianli	
	Water Level (m)	Discharge (m^3 s^{-1})	Water Level (m)	Discharge (m^3 s^{-1})
21 June 2024 08:00:00	32.71	N/A	30.87	16,500
21 June 2024 14:00:00	32.88	N/A	31.05	16,700
22 June 2024 08:00:00	33.37	N/A	31.55	17,500
22 June 2024 14:00:00	33.49	N/A	31.67	17,800
23 June 2024 08:00:00	33.63	N/A	31.92	17,700
23 June 2024 14:00:00	33.7	N/A	31.99	17,500

Appendix B. Sensitivity Comparison of Temporal Rainfall-Forcing Treatments

To examine the numerical behavior of different temporal treatments for 6 min rainfall forcing, a sensitivity comparison was conducted among stepwise input, linear interpolation,

conventional cubic spline interpolation, and monotone PCHIP/Fritsch–Carlson interpolation. The comparison focused on four diagnostic aspects: the generation of negative rainfall, overshoot beyond the original rainfall nodes, conservation of accumulated rainfall, and TELEMAC-2D convergence status. The purpose of this comparison was not to replace the native rainfall-input mechanism of TELEMAC-2D, but to evaluate how different temporal treatments affect the stability and physical consistency of the rainfall source term under second- or sub-second hydrodynamic time steps.

Table A5. Diagnostic comparison of different temporal rainfall-forcing treatments for TELEMAC-2D coupling.

Temporal Forcing Treatment	Negative Rainfall	Overshoot Beyond Original Rainfall Nodes	Accumulated Rainfall Conservation	TELEMAC-2D Convergence Status
Stepwise input	No	No	Conserved	May exceed maximum iteration count during intense rainfall
Linear interpolation	No	No	Conserved after interval-wise normalization	Stable
Conventional cubic spline interpolation	Possible	Possible	Not strictly guaranteed without correction	Stable but physically less constrained
Monotone PCHIP/Fritsch–Carlson interpolation	No	No	Conserved after interval-wise normalization	Stable

References

1. Seneviratne, S.I.; Zhang, X.; Adnan, M.; Badi, W.; Dereczynski, C.; Luca, A.D.; Ghosh, S.; Iskandar, I.; Kossin, J.; Lewis, S. Weather and climate extreme events in a changing climate. In *Climate Change 2021: The Physical Science Basis: Working Group I Contribution to the Sixth Assessment Report of the Intergovernmental Panel on Climate Change*; Cambridge University Press: Cambridge, UK, 2021; pp. 1513–1766.
2. Trenberth, K.E. The impact of climate change and variability on heavy precipitation, floods, and droughts. In *Encyclopedia of Hydrological Sciences*; John Wiley & Sons, Ltd.: Hoboken, NJ, USA, 2005; Volume 17, pp. 1–11.
3. Bauer, P.; Thorpe, A.; Brunet, G. The quiet revolution of numerical weather prediction. *Nature* **2015**, *525*, 47–55. [CrossRef] [PubMed]
4. Zheng, Y.; Zhang, X.; Zhou, Q.; Duan, Y.; Chen, Y.; He, L. Progress and Challenges in Operational Nowcasting Techniques for Severe Convective Weather. *Meteorol. Mon.* **2010**, *36*, 33–42.
5. Costabile, P.; Costanzo, C.; Kalogiros, J.; Bellos, V. Toward street-level nowcasting of flash floods impacts based on HPC hydrodynamic modeling at the watershed scale and high-resolution weather radar data. *Water Resour. Res.* **2023**, *59*, e2023WR034599. [CrossRef]
6. Schmid, F.; Wang, Y.; Harou, A. Nowcasting guidelines—A summary. *WMO Bull.* **2019**, *68*, 63–68.
7. De Luca, D.L.; Capparelli, G. Rainfall nowcasting model for early warning systems applied to a case over Central Italy. *Nat. Hazards* **2022**, *112*, 501–520. [CrossRef]
8. Dai, K.; Chen, J.; Yang, X. Focusing on Kilometer and Minute-level Key Technologies to Improve Accurate Forecasting of Hazardous Weather. *China Disaster Reduct.* **2023**, *9*, 34–37.
9. Pulkkinen, S.; Nerini, D.; Pérez Hortal, A.A.; Velasco-Forero, C.; Seed, A.; Germann, U.; Foresti, L. Pysteps: An open-source Python library for probabilistic precipitation nowcasting (v1. 0). *Geosci. Model Dev.* **2019**, *12*, 4185–4219. [CrossRef]
10. Woo, W.-c.; Wong, W.-k. Operational application of optical flow techniques to radar-based rainfall nowcasting. *Atmosphere* **2017**, *8*, 48. [CrossRef]
11. Shi, X.; Chen, Z.; Wang, H.; Yeung, D.-Y.; Wong, W.-K.; Woo, W.-c. Convolutional LSTM network: A machine learning approach for precipitation nowcasting. In *Proceedings of the 29th International Conference on Neural Information Processing Systems, Montreal, QC, Canada, 7–12 December 2015*; MIT Press: Cambridge, CA, USA, 2015; Volume 28.
12. Shi, X.; Gao, Z.; Lausen, L.; Wang, H.; Yeung, D.-Y.; Wong, W.-k.; Woo, W.-c. Deep learning for precipitation nowcasting: A benchmark and a new model. *Adv. Neural Inf. Process. Syst.* **2017**, *30*, 5618–5628.
13. Albu, A.-I.; Czibula, G.; Mihai, A.; Czibula, I.G.; Burcea, S.; Mezghani, A. Nextnow: A convolutional deep learning model for the prediction of weather radar data for nowcasting purposes. *Remote Sens.* **2022**, *14*, 3890. [CrossRef]

14. She, L.; Zhang, C.; Man, X.; Shao, J. LLMDiff: Diffusion model using frozen LLM transformers for precipitation nowcasting. *Sensors* **2024**, *24*, 6049. [CrossRef]
15. Imhoff, R.O.; Brauer, C.C.; van Heeringen, K.-J.; Uijlenhoet, R.; Weerts, A.H. Large-sample evaluation of radar rainfall nowcasting for flood early warning. *Water Resour. Res.* **2022**, *58*, e2021WR031591. [CrossRef]
16. Gao, Z.; Shi, X.; Han, B.; Wang, H.; Jin, X.; Maddix, D.; Zhu, Y.; Li, M.; Wang, Y.B. Prediff: Precipitation nowcasting with latent diffusion models. *Adv. Neural Inf. Process. Syst.* **2023**, *36*, 78621–78656.
17. Ravuri, S.; Lenc, K.; Willson, M.; Kangin, D.; Lam, R.; Mirowski, P.; Fitzsimons, M.; Athanassiadou, M.; Kashem, S.; Madge, S. Skilful precipitation nowcasting using deep generative models of radar. *Nature* **2021**, *597*, 672–677. [CrossRef]
18. Paschalis, A.; Fatichi, S.; Molnar, P.; Rimkus, S.; Burlando, P. On the effects of small scale space–time variability of rainfall on basin flood response. *J. Hydrol.* **2014**, *514*, 313–327. [CrossRef]
19. Saharia, M.; Kirstetter, P.E.; Vergara, H.; Gourley, J.J.; Emmanuel, I.; Andrieu, H. On the impact of rainfall spatial variability, geomorphology, and climatology on flash floods. *Water Resour. Res.* **2021**, *57*, e2020WR029124. [CrossRef]
20. Open TELEMAC-MASCARET Consortium. *TELEMAC-2D User Manual, Version 9.0*; EDF: Chatou, France, 2024.
21. Li, Z.; Liu, J.; Mei, C.; Shao, W.; Wang, H.; Yan, D. Comparative analysis of building representations in TELEMAC-2D for flood inundation in idealized urban districts. *Water* **2019**, *11*, 1840. [CrossRef]
22. Lazzarin, T.; Costabile, P.; Viero, D. An efficient physics-based modeling strategy for pluvial floods in urban areas with a subgrid scheme for the stormwater drainage network. *J. Hydrol.* **2025**, *661*, 133617. [CrossRef]
23. Godara, N.; Bruland, O.; Alfredsen, K. Comparison of two hydrodynamic models for their rain-on-grid technique to simulate flash floods in steep catchment. *Front. Water* **2024**, *6*, 1384205.
24. Reinert, J.; Hofmann, J.; Almoradie, A.; Brüll, C. Assessing the Challenges of Urban Flood Modelling: A TELEMAC-2D Rain-on-Grid Framework to Quantify the Relative Impacts of Surface Calibration, Infrastructure Modelling and Operational Rules in the Emscher Catchment. *Water* **2026**, *18*, 1224. [CrossRef]
25. Perrini, P.; Cea, L.; Chiaravalloti, F.; Gabriele, S.; Manfreda, S.; Fiorentino, M.; Gioia, A.; Iacobellis, V. A runoff-on-grid approach to embed hydrological processes in shallow water models. *Water Resour. Res.* **2024**, *60*, e2023WR036421. [CrossRef]
26. Godara, N.; Bruland, O.; Alfredsen, K. Modelling flash floods driven by rain-on-snow events using rain-on-grid technique in the hydrodynamic model TELEMAC-2D. *Water* **2023**, *15*, 3945. [CrossRef]
27. Toro, E.F. *Shock-Capturing Methods for Free-Surface Shallow Flows*; Wiley and Sons Ltd.: Hoboken, NJ, USA, 2001.
28. Burden, R.L.; Faires, J.D.; Toomey, H.A. *Numerical Analysis Algorithms in C*; Brooks Cole: Pacific Grove, CA, USA, 1997.
29. Bellos, V.; Costanzo, C.; Kalogiros, J.; Ahmadian, R.; Rozos, E.; Costabile, P. Nowcasting Floods in Detailed Scales Considering the Uncertainties Associated with impact-based Practical Applications. *Water Resour. Manag.* **2025**, *39*, 4205–4225. [CrossRef]
30. Zhang, F.; Zhang, Q.; Sun, J.; Xu, J. Convection initiation during the Meiyu environment in the Yangtze-Huai River Basin of China. *J. Geophys. Res. Atmos.* **2023**, *128*, e2022JD038077. [CrossRef]
31. Zhu, R.; Chen, L. Climatic characteristics of the Jianghuai cyclone and its linkage with precipitation during the Meiyu period from 1961 to 2020. *Nat. Hazards Earth Syst. Sci.* **2024**, *24*, 1937–1950. [CrossRef]
32. Takaku, J.; Tadono, T.; Doutsu, M.; Ohgushi, F.; Kai, H. Updates of 'AW3D30'ALOS global digital surface model in Antarctica with other open access datasets. *Int. Arch. Photogramm. Remote Sens. Spat. Inf. Sci.* **2021**, *43*, 401–408. [CrossRef]
33. Yang, J.; Huang, X. The 30 m annual land cover dataset and its dynamics in China from 1990 to 2019. *Earth Syst. Sci. Data* **2021**, *13*, 3907–3925. [CrossRef]
34. Yang, J.; Huang, X. The 30 m annual land cover datasets and its dynamics in China from 1985 to 2024. *Earth Syst. Sci. Data* **2025**, *13*, 3907–3925. [CrossRef]
35. Li, W. *Hydraulic Calculation Manual*, 2nd ed.; Water & Power Press: Beijing, China, 2006. (In Chinese)
36. Yu, D.; Li, X.; Ye, Y.; Zhang, B.; Luo, C.; Dai, K.; Wang, R.; Chen, X. Diffcast: A unified framework via residual diffusion for precipitation nowcasting. In Proceedings of the IEEE/CVF Conference on Computer Vision and Pattern Recognition, Seattle, WA, USA, 16–22 June 2024; pp. 27758–27767.
37. Sohl-Dickstein, J.; Weiss, E.; Maheswaranathan, N.; Ganguli, S. Deep unsupervised learning using nonequilibrium thermodynamics. In Proceedings of the International Conference on Machine Learning, Lille, France, 6–11 July 2015; pp. 2256–2265.
38. Chenmin, N.; Marsani, M.F.; Pei Shan, F. Flood prediction based on feature selection and a hybrid deep learning network. *J. Water Clim. Change* **2024**, *15*, 1245–1261. [CrossRef]
39. Lazzarin, T.; Xu, L.; Yuan, S.; Hoitink, A.; Viero, D. Accounting for density-driven secondary flows at river confluences with a 2-D depth-averaged hydro-morphodynamic model. *Environ. Model. Softw.* **2025**, *195*, 106735. [CrossRef]
40. Fritsch, F.N.; Carlson, R.E. Monotone piecewise cubic interpolation. *SIAM J. Numer. Anal.* **1980**, *17*, 238–246. [CrossRef]
41. Costabile, P.; Lombardo, M.; Costanzo, C.; Tsoukalas, I.; Bellos, V. A Stochastic Rain-on-Grid Framework for Handling Spatio-Temporal Rainfall Uncertainty in Impact-based Flood Nowcasting. *Int. J. Disaster Risk Reduct.* **2026**, *134*, 105998. [CrossRef]
42. Higham, D.J. Monotonic piecewise cubic interpolation, with applications to ODE plotting. *J. Comput. Appl. Math.* **1992**, *39*, 287–294. [CrossRef]

43. Huynh, H.T. Accurate monotone cubic interpolation. *SIAM J. Numer. Anal.* **1993**, *30*, 57–100. [CrossRef]
44. Moriasi, D.N.; Arnold, J.G.; Van Liew, M.W.; Bingner, R.L.; Harmel, R.D.; Veith, T.L. Model evaluation guidelines for systematic quantification of accuracy in watershed simulations. *Trans. ASABE* **2007**, *50*, 885–900. [CrossRef]

Disclaimer/Publisher's Note: The statements, opinions and data contained in all publications are solely those of the individual author(s) and contributor(s) and not of MDPI and/or the editor(s). MDPI and/or the editor(s) disclaim responsibility for any injury to people or property resulting from any ideas, methods, instructions or products referred to in the content.